Available online at www.sciencedirect.com
ScienceDirect
Journal of Power Sources 175 (2008) 75–81
JOURNAL OF POWER SOURCES
www.elsevier.com/locate/jpowsour

Thermal stabilities of nanoporous metallic electrodes at elevated temperatures

Xiaohong Wang [a], Hong Huang [b,e,*,1], Tim Holme [b], Xu Tian [c], Fritz B. Prinz [b,d]

[a] *Institute of Microelectronics, Tsinghua University, Beijing, China*
[b] *Department of Mechanical Engineering, Stanford University, Stanford, USA*
[c] *Department of Applied Physics, Stanford University, Stanford, USA*
[d] *Department of Materials Science and Engineering, Stanford University, Stanford, USA*
[e] *Department of Mechanical and Materials Engineering, Wright state University, Dayton, USA*

Received 6 July 2007; received in revised form 14 September 2007; accepted 17 September 2007
Available online 29 September 2007

Abstract

Currently Pt-based metals are the best catalytic electrodes for fuel cells at operating temperatures below 500 °C. Pure platinum electrodes suffer degradation of microstructure over time at elevated temperatures due to Ostwald ripening. In this paper, better thermal stability of Pt–Ni nanoporous thin films relative to pure Pt is reported. Based on *ab initio* calculations, it was found that both the surface energy of a $Pt_{0.7}Ni_{0.3}$ cluster and the energy change of the Pt–Ni alloy cluster upon ripening on yttria stabilized zirconia (YSZ) solid electrolyte were lower than pure Pt. This suggested a better thermal stability of $Pt_{0.7}Ni_{0.3}$ than Pt. In addition, annealing impacts on microstructures and properties of nanoporous Pt and Pt–Ni alloy thin films were examined experimentally. SEM images show dramatic porosity reduction for pure Pt after annealing at temperatures of 400–600 °C but insignificant microstructure change for Pt–Ni nanoporous thin films. As a result, in solid oxide fuel cells using nanoporous Pt–Ni cathodic catalysts instead of pure Pt, better stability, lower electrode impedances, and higher power densities were achieved at elevated operating temperatures (350–500 °C).
© 2007 Elsevier B.V. All rights reserved.

Keywords: Fuel cell; Thermal stability; Porous thin film; Catalyst; Alloy

1. Introduction

Fuel cells are attractive because of their potential high efficiency and environmental friendliness. Currently, polymer electrolyte membrane fuel cells (PEMFCs) and solid oxide fuel cells (SOFCs) are the subject of extensive studies [1]. PEMFCs must be operated below 100 °C in order to avoid dry-out of water in the polymeric electrolyte [2], while SOFCs must be operated above 700 °C due to the limited ionic conductivity in ceramic electrolyte [3]. The operating temperature constraints limit wide applications of fuel cells. Reduction of SOFCs' operating temperatures is under active investigation [3–6]. Typical ceramic cathodic materials for SOFCs include strontium-doped lanthanum manganite (LSM) and lanthanum strontium cobaltite ferrite (LSCF). At intermediate temperature (500–700 °C) significant increase in cathode polarization was reported in SOFCs with such cathodes as a result of high activation energy (1.5–2.0 eV) [7,8]. Consequently, these oxide cathodes are no longer suitable for SOFCs upon further decreasing temperatures well below 500 °C. Presently, Pt-based metals are still the best catalysts for LT-SOFCs [9]. Huang et al. [10] recently has successfully demonstrated Ultra-Thin SOFCs (UTSOFC) and achieved a peak power density of 130 mW cm^{-2} at 350 °C. The UT-SOFC architecture was made of 50 nm thick dense yttria stabilized zirconia (YSZ) electrolyte membrane sandwiched between 80 nm thick nanoporous Pt used as cathode and anode. In contrast, an UTSOFC consisting of 100 nm thick LSCF cathode

* Corresponding author at: Rapid Prototyping Laboratory, Department of Mechanical Engineering, Stanford University, 440 Escondido Mall, Stanford, CA 94305, USA. Tel.: +1 650 7231301; fax: +1 650 7235034.
E-mail address: hong.huang@wright.edu (H. Huang).
[1] Present address (effective September 1, 2007): Department of Mechanical and Materials Engineering, Wright State University, 3640 Colonel Glenn Highway, Dayton, OH 45435, USA. Tel.: +1 937 7753982, fax: +1 937 7755040.

0378-7753/$ – see front matter © 2007 Elsevier B.V. All rights reserved.
doi:10.1016/j.jpowsour.2007.09.066

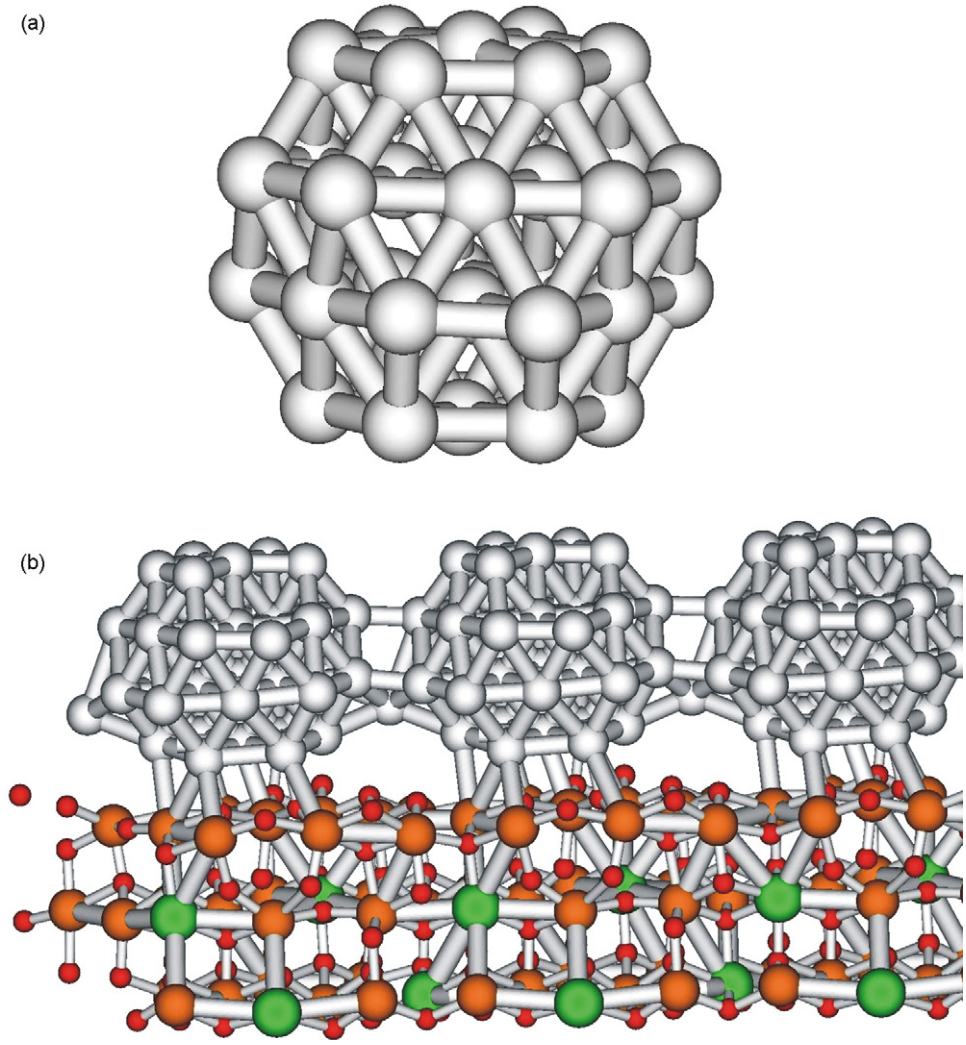

Fig. 1. (a) Pt_{38} cluster after relaxation in vacuum. Termination is by low energy (1 1 1) and (1 0 0) planes; (b) three supercells of Pt_{38}/YSZ after a Pt atom has been removed from the top corner of the cluster and placed between neighboring clusters. Pt atoms shown in grey, Zr in brown, O in red, and Y in green. (For interpretation of the references to color in this figure legend, the reader is referred to the web version of the article.)

exhibited much larger cathode polarization leading to several orders of magnitude lower in terms of peak power density [11].

However, pure platinum electrode suffers degradation of microstructure over time resulting from Ostwald ripening or so-called coarsening. In PEMFCs it is often reported that performance gradually degrades as a result of coarsening of nano-Pt grains supported on carbon, which is commonly used as catalytic cathode [12,13]. The coarsening impact becomes more severe upon increasing operating temperature, as observed in the automobile three-way catalysts [14] and UTSOFCs operated at temperatures of 250–450 °C. In order to prevent the Ostwald ripening and hence improve electrode stability extensive research proceeded towards developing Pt-based alloy electrode in PEMFCs. Additionally, improved catalytic activity for oxygen reduction was observed by using Pt–M (M = Ni, Co, Mn, Fe, V, Cr, Ir) [12,15–17]. From these points of views we investigated thermal stability as well as catalytic activity of Pt–M compared with pure Pt aiming to improve LT-SOFC performance. Based on quantum simulation surface energy and energy change of $Pt_{0.7}Ni_{0.3}$ cluster on yttria stabilized zirco-

Table 1
Deposition rate and composition of Pt–Ni via co-sputtering

The number of Ni pieces on the Pt target	Deposition rate (nm s^{-1})	Pt composition in Pt–Ni alloys (%)
6	0.7	70
4	1.2	84
3	1.3	89
2	1.5	94
1	1.7	97
0	1.8	100

Table 2
Surface energies and energy changes as a result of "ripening" for the different clusters considered

	Pt_{38}	$Pt_{0.7}Ni_{0.3}$
γ (eV $atom^{-1}$)	2.2	2.2
ΔE (eV)	−0.72	−0.65

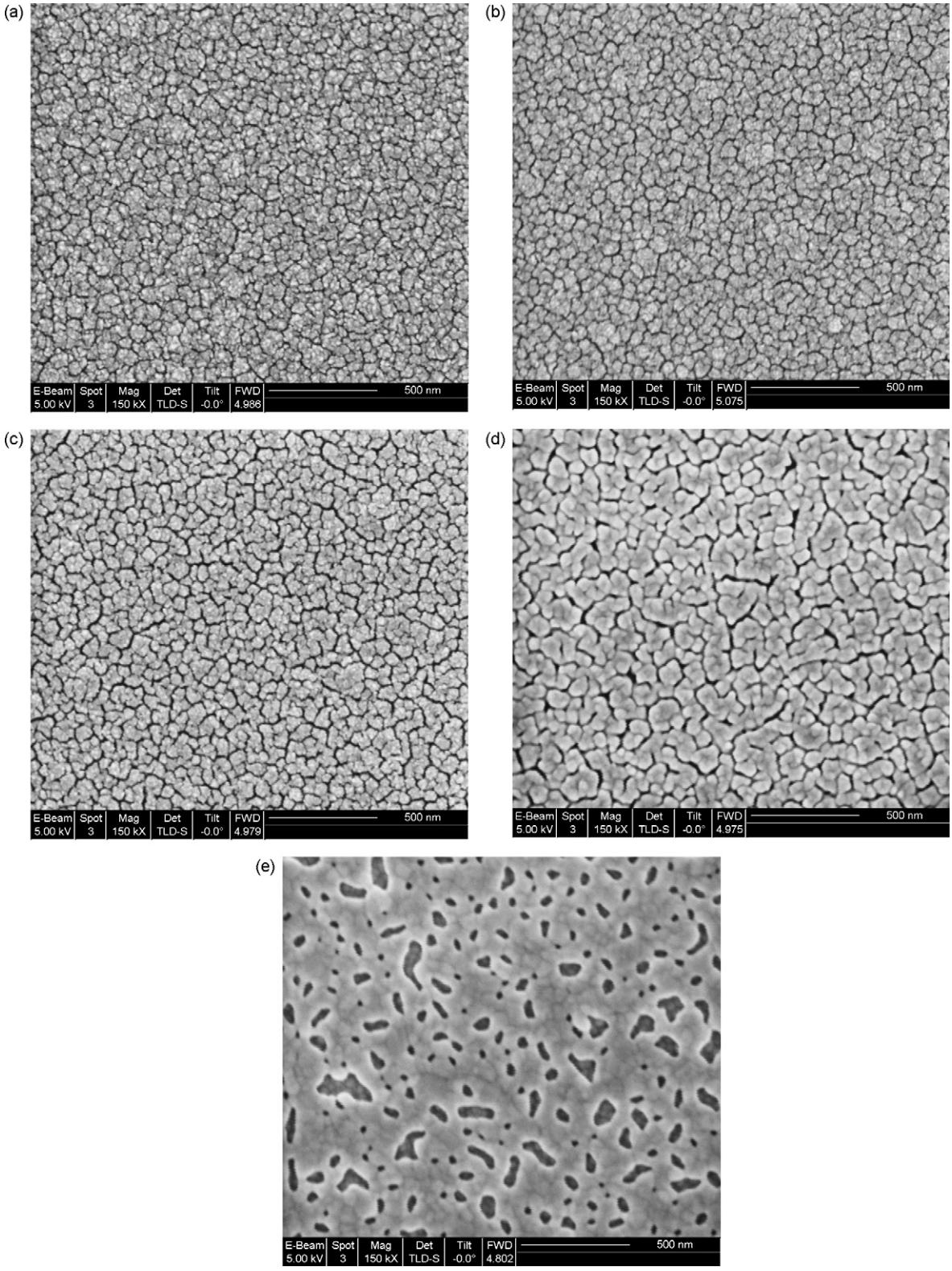

Fig. 2. SEM images of 80 nm thick Pt films deposited on Si substrate before and after annealing at elevated temperatures for 2 h. (a) As-deposited; (b) 350 °C; (c) 400 °C; (d) 500 °C, and (e) 600 °C.

nia (YSZ) solid electrolyte upon coarsening were computed and compared with pure Pt. Experimentally, we monitored morphology changes of pure Pt and Pt–Ni nanoporous thin films as a function of annealing temperature. Furthermore, current–voltage characteristics of SOFCs and the electrode polarization resistances were evaluated in the temperature range of 350–550 °C. These results will be presented in this paper.

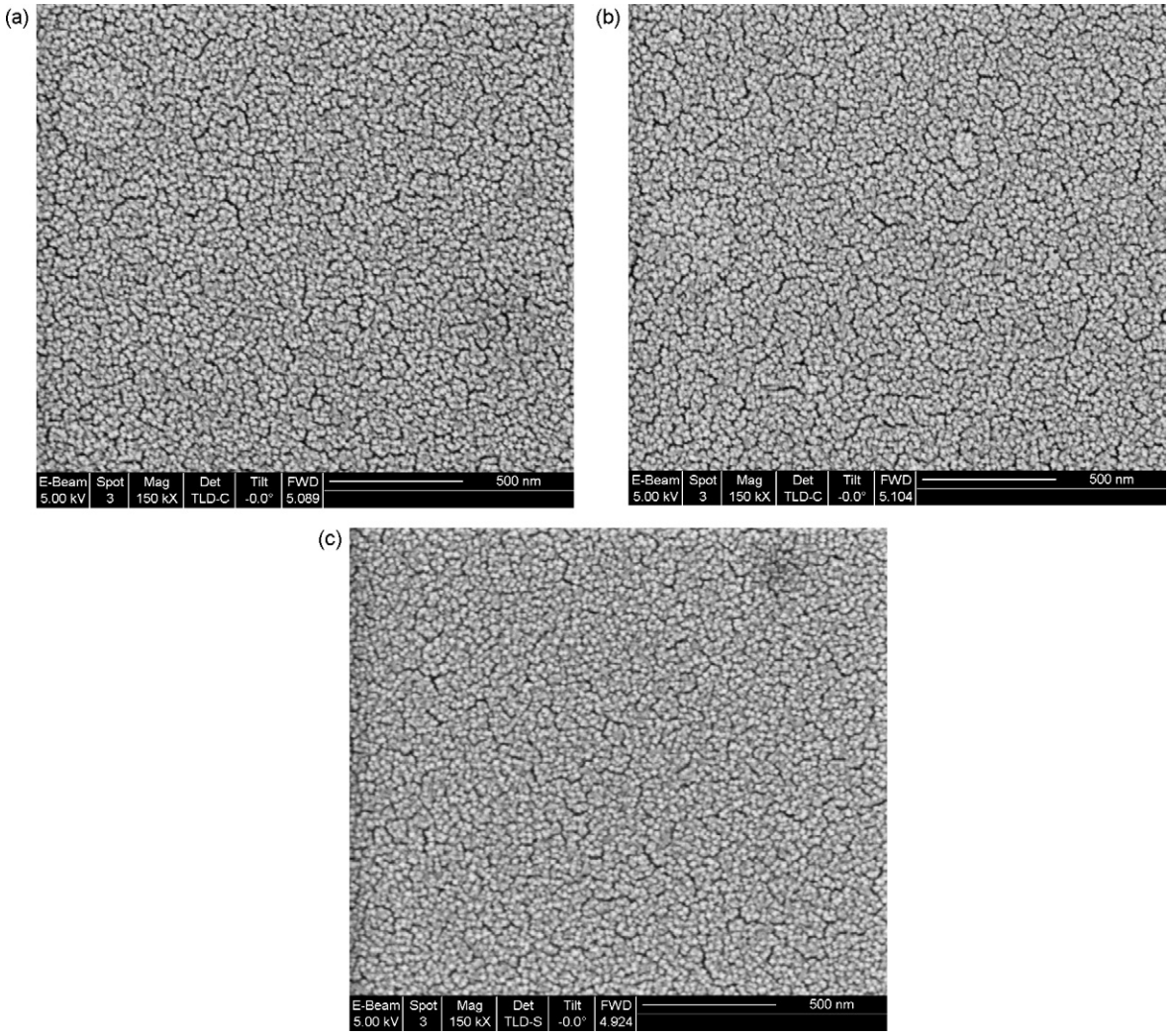

Fig. 3. SEM images of 80 nm thick $Pt_{0.84}Ni_{0.16}$ films deposited on Si substrate before anneal and after annealing at elevated temperatures for 2 h. (a) As-deposited; (b) 350 °C, and (c) 600 °C.

2. Quantum simulation

The *ab initio* code VASP was used for all the following calculations [18]. Electronic states were expanded in plane waves with energy cutoffs of 300 eV. A Monkhorst-Pack [19] $2 \times 2 \times 1$ k-point sampling scheme was used; convergence with regard to the number of k-points was tested and found to be adequate for the relatively large supercell used in the calculations. Ultrasoft pseudopotentials in the GGA scheme were used with the Perdew-Wang 91 exchange correlation functional [20]. Methfessel-Paxton order 1 smearing was used with a smearing width of 0.2 eV. A Pt_{38} cluster, shown in Fig. 1(a), terminated by low energy (1 1 1) and (1 0 0) planes was constructed as a model for nanoparticle catalysts. The same size of a Pt–Ni alloy cluster with a composition of $Pt_{0.7}Ni_{0.3}$ was formed by randomly substituting a given number of Ni atoms for the host Pt atoms. The "apparent" surface energy (γ, eV atom^{-1}) of the nanoparticle was calculated based on the following formula:

$$\gamma = \frac{E_{\text{Pt-Ni,alloy}} - e_{\text{Ni,bulk}} \times N_{\text{Ni}} - e_{\text{Pt,bulk}} \times N_{\text{Pt}}}{N_{\text{Ni}} + N_{\text{Pt}}}$$

$E_{\text{Pt–Ni,alloy}}$ is the total energy of the alloyed nanoparticle after relaxation in vacuum. N_{Ni} and N_{Pt} are the numbers of Ni dopant and Pt host atoms, respectively, and $e_{\text{Ni(Pt),bulk}}$ is the energy per atom of the dopant (host) bulk crystal at the lattice constant which minimizes the energy of the system. Note that in the case of Pt, γ is a true surface energy, while in the case of Pt–Ni alloys γ includes a contribution from the enthalpy of mixing.

A model for ripening was constructed by placing the above nanoclusters on a slab of YSZ, a common electrolyte in SOFCs, as shown in Fig. 1(b). The YSZ slab was constructed by randomly substituting four Y atoms in Zr cation sites and removing two O atoms to create vacancies at the same time to preserve electroneutrality of the system. Relaxation of the atoms was allowed. To simulate the ripening process, a Pt atom was removed

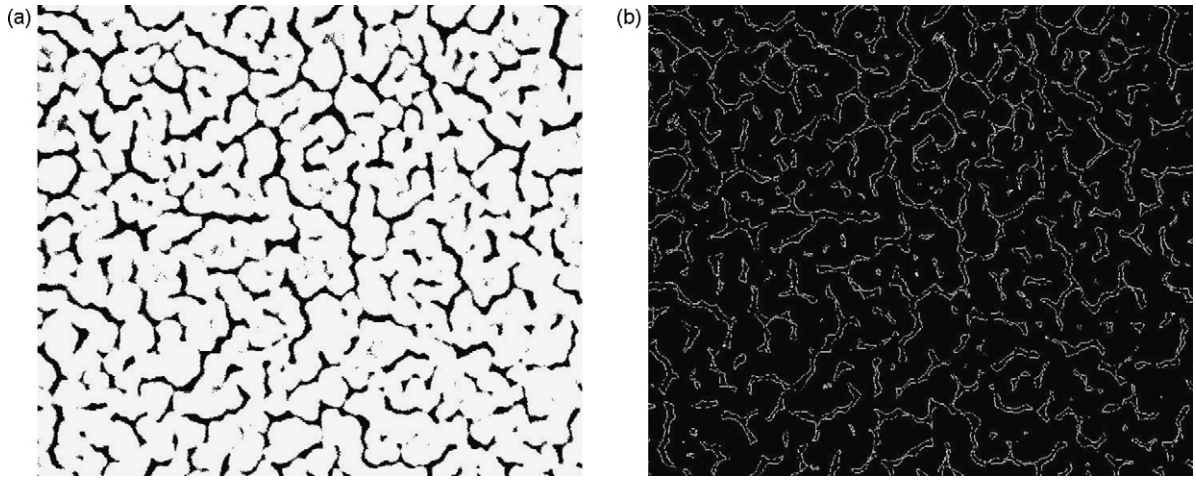

Fig. 4. Morphology of 80 nm Pt after annealed at 500 °C for 2 h. (a) Contrast-adjusted SEM image ready for digital processing, and (b) binary image converted from (a).

from the top of the cluster and placed between neighboring clusters, the energy difference between the two configurations was considered to be the thermodynamic driving force for ripening.

3. Experimental aspects

Nanoporous Pt and Pt–Ni alloy thin films were DC-sputtered on two different substrates, a Si wafer with a 500 nm silicon nitride passivation layer and a microcrystalline YSZ electrolyte plate (Ceraflex). The sputtering materials were from Kurt Lesker Co. with a purity of 99.99%. The sputtering conditions for thin porous Pt electrodes were 10 Pa (chamber pressure) at a power of 100 W for 80 s. The deposition rate was estimated at 1 nm s^{-1}. For Pt–Ni alloy thin films, appropriate quantities of nickel pieces were homogeneously distributed over the Pt target. The number of nickel pieces correlated with Ni content in the alloy films. Since the deposition rate of Pt–Ni slightly decreased upon increasing Ni content, sputtering time was adjusted accordingly in order to achieve same thickness films at the same chamber pressure. Compositions and oxidation state of Pt and Pt–Ni samples at the surface and in depth were analyzed by using X-ray photoelectron spectroscopic (XPS) techniques. Table 1 lists the deposition rate of Pt–Ni with different compositions.

Scanning electron microscopy (FEI Strata 235DB dual-beam FIB/SEM) was used to monitor microstructure changes of Pt and Pt–Ni nanoporous thin films after annealing at different temperatures. The as-deposited samples were annealed at temperatures between 350 and 600 °C for 2 h in a tube furnace. The heating rate was set at 10 °C min^{-1} while the cooling rate was 20 °C min^{-1}. SEM images were then processed using MATLAB software to quantify the edges of visible pores, which are associated with the length of gas/electrolyte/electrode three phase boundaries (TPB). The processing steps include (1) reading the image and adjusting its contrast; (2) converting a gray scale image to a binary image; (3) identifying the edges in a binary image and (4) counting the numbers of pixel in the edges in the binary image.

Characteristics of the fuel cells with Pt and Pt–Ni alloy cathodes were investigated. The fuel gas was pure hydrogen and the oxidant gas was air. Fuel cells were constructed by using 50 μm thick microcrystalline YSZ electrolyte (provided by Ceraflex Co.), 80 nm thick nanoporous Pt anode, but different nanoporous cathodes, i.e., Pt, $Pt_{0.84}Ni_{0.16}$, and $Pt_{0.7}Ni_{0.3}$, etc. All the cathodes, sputtered at the previously described conditions, have the same thicknesses and initial microstructures. Current–voltage curves were recorded at temperatures of 400 °C on a Solartron 1260/1287 in galvanodynamic (scanning current) mode. Furthermore, electrochemical impedance spectroscopy was used to evaluate electrode polarization resistances. Electrochemical impedance spectra (EIS) were recorded at 0.5 V vs. the reference anodic electrode at 400 °C. The AC amplitude was 50 mV and the frequency sweeps between 100 mHz and 1 MHz. The EIS results were analyzed by using Z-plot software based on complex nonlinear least squares fitting.

4. Results and discussion

Table 2 lists the simulated surface energies (γ) of Pt and $Pt_{0.7}Ni_{0.3}$ clusters consisting of 38 atoms. Note that in the case of Pt, γ_{Pt} is a true surface energy, while in the case of Pt–Ni alloys $\gamma_{Pt–Ni}$ includes a contribution from the enthalpy of mixing to form the alloy. If this mixing enthalpy was subtracted from the computed value, the actual surface energy of Pt–Ni is expected to be lower than pure Pt. Table 2 also lists the energy changes from modeling ripening process. A smaller energy difference before and after ripening is obtained for Pt–Ni alloy relative to pure Pt. Both results suggest that Pt–Ni alloy clusters are relatively more stable compared with pure Pt. As consistent trends were observed from both methods, the former calculation might be an effective method for screen candidate catalysts in terms of thermal stability since the ripening calculation is much more computationally demanding.

SEM images of as-deposited Pt electrodes as well as those annealed at different temperatures are exhibited in Fig. 2. As can be seen from Fig. 2(a), the as-deposited Pt thin film by DC

sputtering is nanoporous and uniform. Individual grain size is around 20 nm in average, and the dimension of each cluster is in the range of 50–100 nm with a gap (pore) of less than 10 nm. The Pt clusters are interconnected which ensure good electrical connection. As a result of annealing at 350 °C for 2 h, Pt clusters begin to agglomerate (see Fig. 2(b)). After annealing at higher temperatures (400 °C and beyond), Pt clusters grow exponentially. As a consequence, most nano-pores between Pt clusters disappear, resulting in fewer, larger pores with a dimension of 100–200 nm, as can be seen in Fig. 2(c–e).

For Pt–Ni thin films, different Ni compositions ranging from 0 to 30 at.% were prepared. According to the phase diagram [21,22], only Pt-based structure exists with Ni doping up to 20 at.%. With higher Ni content there may exist ordered Pt_3Ni phase. Morphologies of the as-deposited and annealed Pt–Ni alloy films with different Ni content prepared in the same conditions are almost identical. In contrast to pure Pt, the morphologies of Pt–Ni alloy thin film changed insignificantly even after annealing at 600 °C. Fig. 3(a–c) presents SEM images of as-deposited $Pt_{0.84}Ni_{0.16}$ thin films, annealed at 350 and 600 °C, respectively. The as-deposited as well as annealed Pt–Ni films are nanoporous and uniform with finer clusters and gaps, similar to the as-deposited pure Pt.

In order to quantify the changes of TPB length, a crucial factor for electrode reaction rate in fuel cells [23], SEM images were processed by using MATLAB software. Fig. 4(a and b) shows a typical contrast-adjusted SEM image and a processed binary image, respectively. The edges in a binary image correspond to edges of the pores in SEM image, which are associated with apparent TPB length. Fig. 5 plots the normalized pixel numbers as a function of annealing temperature. As can be seen, the apparent TPB length in Pt films decreased exponentially above 400 °C, and approximate 80% active TPBs were lost after annealing at 600 °C. For Pt–Ni samples, in contrast, the TPB length was maintained at the same level even after annealing at 600 °C. Clearly, these results indicate that Pt–Ni alloys have better capabilities to resist coarsening and hence maintain their original microstructures under thermal impacts. This result is consistent with the quantum simulation prediction.

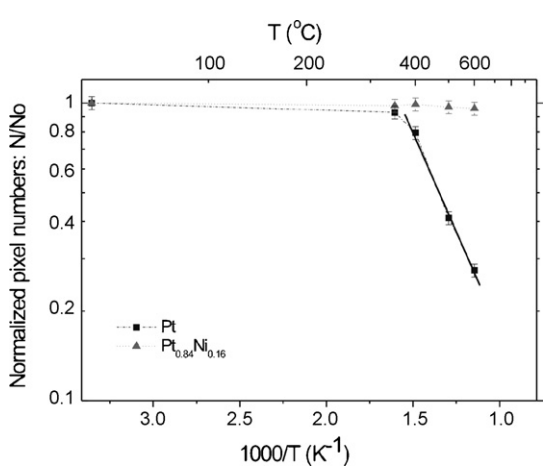

Fig. 5. Normalized pixel numbers associated with TPB length as a function of annealing temperature.

It is well known that smaller clusters tend to grow into larger clusters. This phenomenon, referred to as ripening, coarsening or sintering, leads to degradation of microstructures and hence catalytic properties over long times and at high temperatures. The basic driving force of ripening is the thermodynamic driving force to minimize the free energy of a system associated with the interfaces. At low temperatures nanoparticles are relatively stable, while above the ripening temperature threshold, nanoparticles tend to grow exponentially as a function of temperature [24]. As can be seen in Fig. 5, the apparent TPB length of Pt as a function of reciprocal annealing temperature shows a plateau followed by a linear increase, characteristic of ripening. Fitting the linear region in the plot provided the ripening activation energy, estimated to be 0.26 eV. It has been reported that energy for adatom formation from kinks is around 0.5–0.6 eV and the adatom diffusion barrier is 0.1–0.2 eV in Ag [25]. The corresponding energy barriers for Pt are expected to be higher than for Ag. According to the ripening activation energy (0.26 eV) observed experimentally, the microstructure change as a result of ripening might be surface diffusion dominant. In quantum simulated ripening process, the energy change (0.75 eV) is the result of moving a Pt atom from the top of the cluster to neighboring clusters, which corroborates with the range of adatom formation energy. Moreover, metal particle growth at elevated temperatures may be more than a physical agglomeration process. Evidence indicates metallic particle growth rate is affected by the substrate and atmosphere. It has been presented previously that Pt sintering proceeded faster in oxidizing atmosphere above 400–500 °C [26,27]. Sintering of Pt in air might also be involved in formation and decomposition process of an oxidic phase such as PtO_2.

To investigate the correlations between morphology changes of Pt and Pt–Ni alloy thin films and electrode properties, fuel cells were fabricated and tested as outlined above. Since the electrolyte and anode were identical for the different samples, any differences in *I–V* characteristics, peak power densities, and electrochemical impedance spectra will lie in their different cathode materials. Fig. 6(a) plots the evolution of the power densities obtained from *I–V* curves recorded over time at 400 °C. For cells with a pure Pt cathode, the power density decreased continuously over time leading to a 20% loss after 60 min testing. In contrast, cells with a Pt–Ni alloy thin film cathode had no decrease of the power density over 1 h. Additionally, an absolute higher power density was observed from $Pt_{0.84}Ni_{0.16}$ alloy cathodes compared to pure Pt. From the impedance spectra presented in Fig. 6(b) the total electrode impedance was reduced two-fold by using $Pt_{0.84}Ni_{0.16}$ alloy cathode. These results suggest that besides better thermal stability, $Pt_{0.84}Ni_{0.16}$ alloy might have higher catalytic activity for oxygen reduction compared with pure Pt. This has been reported in PEMFCs operated below 100 °C [12,16]. Details on the improved catalytic activity of Pt–Ni relative to Pt in LT-SOFCs are still under investigation. For $Pt_{0.7}Ni_{0.3}$ cathodes, on the one hand, better thermal stability than Pt was observed. This is the same as $Pt_{0.84}Ni_{0.16}$ alloy and consisted with quantum prediction. On the other hand, lower power densities using $Pt_{0.7}Ni_{0.3}$ than using Pt and $Pt_{0.84}Ni_{0.16}$ cathodes were observed. XPS results indicated emergence of a

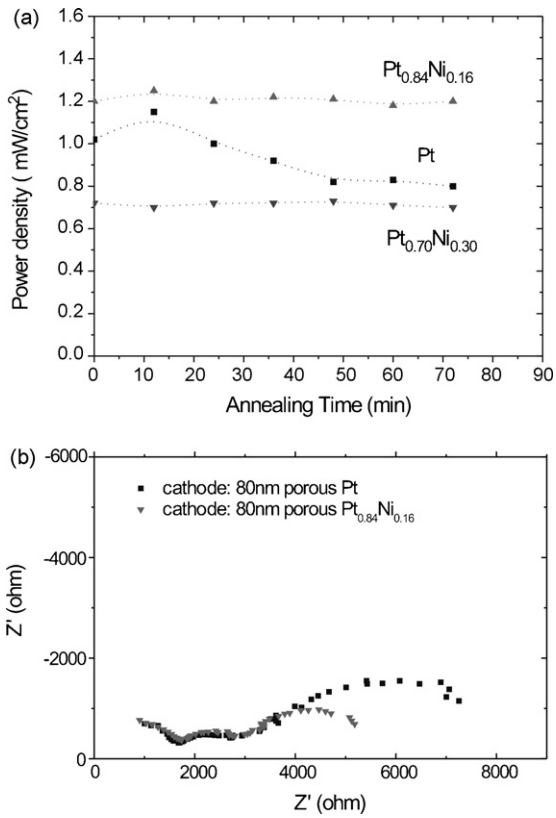

Fig. 6. (a) Evolution of the power densities obtained at 0.4 V over times at 400 °C operating temperature in SOFCs consisting of 50 um thick microcrystalline YSZ electrolyte and 80 nm thick nanoporous Pt anode but 80 nm thick different nanoporous cathodes, i.e., Pt, $Pt_{0.84}Ni_{0.16}$, and $Pt_{0.7}Ni_{0.3}$, etc., and (b) electrochemical impedance spectra of the fuel cells at 0.5 V vs. anodic reference electrode after a 1 h performance evaluation at 400 °C.

small portion of nickel oxide in this $Pt_{0.7}Ni_{0.3}$ cathode after fuel cell testing, which may significantly slow down oxygen reduction process leading to low power density. Hence, optimal Pt–Ni composition is necessary to achieve both thermal stability and catalytic activity for LT-SOFCs.

5. Conclusions

Quantum calculations on Pt and Pt–Ni clusters and experimental observations on nanoporous thin films indicated better thermal stabilities of Pt–Ni alloys relative to pure Pt. At room temperature, morphologies of as-deposited Pt and Pt–Ni nanoporous thin films via DC sputtering were similar. However, after annealing at high temperatures, particularly above 400 °C, the morphology of Pt changed significantly. After annealing at 600 °C for 2 h approximately 80% of active TPB was lost. The microstructure changes resulting from ripening led to fuel cell performance degradation. In contrast, Pt–Ni alloy nanoporous thin films maintained their as-deposited morphologies even after annealing at 600 °C. As a result, power density changed insignificantly over time at 400 °C operating temperature.

Acknowledgements

T. Holme is indebted to Kai Fan for initial work on the calculations. Calculations were performed using TeraGrid resources provided by SDSC and NCSA, funded by the National Science Foundation.

References

[1] B.C.H. Steele, A. Heizel, Nature 414 (2001) 345.
[2] G. Alberti, M. Cosciola, Annu. Rev. Mater. Res. 33 (2003) 129.
[3] B.P. Brandon, S. Skinner, B.C.H. Steele, Annu. Rev. Mater. Res. 33 (2003) 183.
[4] S. Souza, S.J. Visco, L.C. De Jonghe, Solid State Ion. 9 (1997) 57.
[5] J.M. Ralph, A.C. Schoeler, M. Krumpelt, J. Mater. Sci. 36 (2001) 1161.
[6] Z. Shao, S.M. Haile, Nature 431 (2004) 170.
[7] S.B. Adler, Chem. Rev. 104 (2004) 4791.
[8] S. Wang, T. Kato, S. Nagata, T. Kaneko, N. Iwashita, T. Honda, M. Dokiya, Solid State Ion. 152–153 (2002) 477.
[9] E.P. Murray, M.J. Sever, S.A. Barnett, Solid State Ion. 148 (2002) 27.
[10] H. Huang, M. Nakamura, P. Su, R. Fasching, Y. Saito, F. Prinz, J. Electrochem. Soc. 154 (2007) B20.
[11] K. Crabb, F. Prinz, Abstract of 16th International Conference on Solid State Ionics, Shanghai, July, 2007.
[12] J. Xie, D.L. Wood, K.L. More, P. Atanassov, R.L. Borup, J. Electrochem. Soc. 152 (2005) A1011.
[13] A.V. Virkar, Y. Zhou, J. Electrochem. Soc. 154 (2007) B540.
[14] Z. Xu, F.S. Xiao, S.K. Purnell, O. Alexeev, S. Kawi, S.E. Deutsch, B.C. Gates, Nature 372 (1994) 346.
[15] L. Xiong, A. Manthiram, J. Electrochem. Soc. 152 (2005) A697.
[16] V. Stamenkovic, B. Mun, K.J.J. Mayrhofer, P.N. Ross, N.M. Markovic, J. Rossmeisl, J. Greeley, J.K. Norskov, Angewandte Chemie 118 (2006) 2963.
[17] Y. Xu, A.V. Ruban, M. Marrikakis, J. Am. Chem. Soc. 126 (2004) 4717.
[18] G. Kresse, J. Hafner, J. Phys. Condens Mater. 6 (1994) 8245.
[19] H. Monkhorst, J. Pack, Phys. Rev. B 13 (1976) 5188.
[20] J. Perdew, J. Chevary, S. Vosko, K. Jackson, M. Pederson, D. Singh, C. Fiolhais, Phys. Rev. B 46 (1992) 6671.
[21] C.E. Dahmani, M.C. Cadeville, J.M. Sanchez, J.L. Moran Lopez, Phys. Rev. Lett. 55 (1985) 1208.
[22] H. Okamoto, Phase Diagrams for Binary Alloys, vol. 1, ASM International, 2000, p. 1.
[23] R. Radhakrishnan, A.V. Virkar, S.C. Singhal, J. Electrochem. Soc. 151 (2005) A927.
[24] H. Brune, Surf. Sci. Rep. 31 (1998) 121.
[25] K. Margenstern, G. Rosenfeld, E. Laesgaard, F. Besenbacher, G. Cosma, Phys. Rev. Lett. 80 (1998) 556.
[26] W.G. Rothschild, H.C. Yao, H.K. Plummer, Langmuir 2 (1986) 588.
[27] H.J. Gruber, J. Phys. Chem. 66 (1962) 48.